



Probing Ultralate Reionization: Direct Measurements of the Mean Free Path over $5 < z < 6$

Downloaded from: <https://research.chalmers.se>, 2025-12-04 22:46 UTC

Citation for the original published paper (version of record):

Zhu, Y., Becker, G., Christenson, H. et al (2023). Probing Ultralate Reionization: Direct Measurements of the Mean Free Path over $5 < z < 6$. *Astrophysical Journal*, 955(2).
<http://dx.doi.org/10.3847/1538-4357/accef4>

N.B. When citing this work, cite the original published paper.



Probing Ultralate Reionization: Direct Measurements of the Mean Free Path over $5 < z < 6$

Yongda Zhu¹, George D. Becker¹, Holly M. Christenson¹, Anson D'Aloisio¹, Sarah E. I. Bosman^{2,3}, Tom Bakx^{4,5,6},
Valentina D'Odorico^{7,8,9}, Manuela Bischetti¹⁰, Christopher Cain¹, Frederick B. Davies², Rebecca L. Davies^{11,12},
Anna-Christina Eilers^{13,23}, Xiaohui Fan¹⁴, Prakash Gaikwad², Martin G. Haehnelt¹⁵, Laura C. Keating¹⁶,
Girish Kulkarni¹⁷, Samuel Lai¹⁸, Hai-Xia Ma⁵, Andrei Mesinger⁸, Yuxiang Qin^{19,12}, Sindhu Satyavolu¹⁷,
Tsutomu T. Takeuchi^{5,20}, Hideki Umehata^{21,22}, and Jinyi Yang¹⁴

¹ Department of Physics & Astronomy, University of California, Riverside, CA 92521, USA; yzhu144@ucr.edu

² Max-Planck-Institut für Astronomie, Königstuhl 17, D-69117, Heidelberg, Germany

³ Institute for Theoretical Physics, Heidelberg University, Philosophenweg 12, D-69120, Heidelberg, Germany

⁴ Department of Space, Earth and Environment, Chalmers University of Technology, Onsala Space Observatory, SE-439 92 Onsala, Sweden

⁵ Division of Particle and Astrophysical Science, Nagoya University, Furo-cho, Chikusa-ku, Nagoya 464-8602, Japan

⁶ National Astronomical Observatory of Japan, 2-21-1, Osawa, Mitaka, Tokyo 181-8588, Japan

⁷ INAF-Osservatorio Astronomico di Trieste, Via Tiepolo 11, I-34143 Trieste, Italy

⁸ Scuola Normale Superiore, Piazza dei Cavalieri 7, I-56126 Pisa, Italy

⁹ IFPU-Institute for Fundamental Physics of the Universe, via Beirut 2, I-34151 Trieste, Italy

¹⁰ Dipartimento di Fisica, Sezione di Astronomia, Università di Trieste, via Tiepolo 11, I-34143 Trieste, Italy

¹¹ Centre for Astrophysics and Supercomputing, Swinburne University of Technology, Hawthorn, Victoria 3122, Australia

¹² ARC Centre of Excellence for All Sky Astrophysics in 3 Dimensions (ASTRO 3D), Australia

¹³ MIT Kavli Institute for Astrophysics and Space Research, 77 Massachusetts Avenue, Cambridge, MA 02139, USA

¹⁴ Steward Observatory, University of Arizona, 933 N. Cherry Avenue, Tucson, AZ 85721, USA

¹⁵ Kavli Institute for Cosmology and Institute of Astronomy, Madingley Road, Cambridge CB3 0HA, UK

¹⁶ Institute for Astronomy, University of Edinburgh, Blackford Hill, Edinburgh EH9 3HJ, UK

¹⁷ Tata Institute of Fundamental Research, Homi Bhabha Road, Mumbai 400005, India

¹⁸ Research School of Astronomy and Astrophysics, Australian National University, Canberra, ACT 2611, Australia

¹⁹ School of Physics, University of Melbourne, Parkville, VIC 3010, Australia

²⁰ The Research Center for Statistical Machine Learning, the Institute of Statistical Mathematics, 10-3 Midori-cho, Tachikawa, Tokyo 190-8562, Japan

²¹ Institute for Advanced Research, Nagoya University, Furo-cho, Chikusa-ku, Nagoya 464-8602, Japan

²² Department of Physics, Graduate School of Science, Nagoya University, Furo-cho, Chikusa-ku, Nagoya 464-8602, Japan

Received 2023 June 19; revised 2023 August 8; accepted 2023 August 8; published 2023 September 25

Abstract

The mean free path of ionizing photons, λ_{mfp} , is a critical parameter for modeling the intergalactic medium (IGM) both during and after reionization. We present direct measurements of λ_{mfp} from QSO spectra over the redshift range $5 < z < 6$, including the first measurements at $z \simeq 5.3$ and 5.6 . Our sample includes data from the XQR-30 VLT large program, as well as new Keck/ESI observations of QSOs near $z \sim 5.5$, for which we also acquire new [C II] $158 \mu\text{m}$ redshifts with ALMA. By measuring the Lyman continuum transmission profile in stacked QSO spectra, we find $\lambda_{\text{mfp}} = 9.33^{+2.06}_{-1.80}$, $5.40^{+1.47}_{-1.40}$, $3.31^{+2.74}_{-1.34}$, and $0.81^{+0.73}_{-0.48}$ pMpc at $z = 5.08$, 5.31 , 5.65 , and 5.93 , respectively. Our results demonstrate that λ_{mfp} increases steadily and rapidly with time over $5 < z < 6$. Notably, we find that λ_{mfp} deviates significantly from predictions based on a fully ionized and relaxed IGM as late as $z = 5.3$. By comparing our results to model predictions and indirect λ_{mfp} constraints based on IGM Ly α opacity, we find that the evolution of λ_{mfp} is consistent with scenarios wherein the IGM is still undergoing reionization and/or retains large fluctuations in the ionizing UV background well below redshift 6.

Unified Astronomy Thesaurus concepts: [Reionization \(1383\)](#); [Intergalactic medium \(813\)](#); [Quasar absorption line spectroscopy \(1317\)](#); [High-redshift galaxies \(734\)](#)

Supporting material: machine-readable table

1. Introduction

When and how reionization occurred is a fundamental question about the early Universe and the first galaxies. The appearance of transmitted flux in the Ly α forest of high-redshift QSOs (e.g., Fan et al. 2006) has long been interpreted as evidence that hydrogen in the intergalactic medium (IGM)

was largely reionized by $z = 6$. In terms of the ionizing photon budget, however, an end of reionization at $z \geq 6$ is challenging to reconcile with a midpoint of $z \sim 7\text{--}8$ suggested by, e.g., observations of the cosmic microwave background (CMB; Planck Collaboration et al. 2020, see also de Belsunce et al. 2021). In particular, star-forming galaxies at $z > 6$ would have to emit ionizing photons extremely efficiently in order to complete reionization within such a short interval. This leaves two possibilities: the ionizing efficiency of galaxies at $z > 6$ is remarkably high, and/or reionization extends to lower redshifts.

A number of observations have now been used to constrain the timeline of reionization. These observations include the

²³ Pappalardo Fellow.



Ly α damping wing in $z \gtrsim 7$ QSO spectra (e.g., Bañados et al. 2018; Davies et al. 2018; Yang et al. 2020a; Wang et al. 2020; Greig et al. 2022), the decline in observed Ly α emission from galaxies at $z > 6$ (e.g., Mason et al. 2018; Hoag 2019; Hu et al. 2019; Mason et al. 2019, and references therein, but see Jung et al. 2020; Wold et al. 2022), and measurements of the thermal state of the IGM at $z > 5$ (e.g., Boera et al. 2019; Gaikwad et al. 2021). These observations support a midpoint of reionization at $z \sim 7$ –8 and are generally consistent with an ending point at $z \sim 6$, as constrained by the fraction of dark pixels in the Ly α forest (e.g., McGreer et al. 2015, but see Zhu et al. 2022).

Other observations, however, suggest that reionization may have extended to significantly lower redshifts. Large-scale fluctuations in the measured Ly α effective optical depth²⁴ (e.g., Fan et al. 2006; Becker et al. 2015; Bosman et al. 2018, 2022; Eilers et al. 2018; Yang et al. 2020b), together with long troughs extending down to or below $z \simeq 5.5$ in the Ly α forest (e.g., Becker et al. 2015; Zhu et al. 2021), potentially indicate the existence of large neutral IGM islands (e.g., Kulkarni et al. 2019; Keating et al. 2020b; Nasir & D’Aloisio 2020; Qin et al. 2021). This interpretation is further supported by dark gaps in the Ly β forest (Zhu et al. 2022). Reionization extending to $z < 6$ is also consistent with the observed underdensities around long dark gaps traced by Ly α -emitting galaxies (Becker et al. 2018; Kashino et al. 2020; Christenson et al. 2021). In addition, such a late-ending reionization scenario is consistent with the evolution of metal-enriched absorbers at $z \sim 6$ (e.g., Becker et al. 2019; Davies et al. 2023a, 2023b), as well as numerical models that reproduce a variety of observations (e.g., Weinberger et al. 2019; Choudhury et al. 2021; Qin et al. 2021; Gaikwad et al. 2023).

A potentially decisive clue for establishing when reionization ended comes from recent measurements of the mean free path of ionizing photons (λ_{mfp}). Becker et al. (2021, hereafter referred to as B21) found that the λ_{mfp} increases by a factor of around 10 between $z = 6.0$ and 5.1 , and λ_{mfp} at $z = 6.0$ is about eight times shorter than what would be expected based on its evolution at $z \lesssim 5$ (see also constraints from Bosman 2021). Such a rapid evolution in λ_{mfp} is expected to occur near the end of reionization due to (i) the growth and merger of ionized bubbles, and (ii) the photoevaporation of dense, optically thick sinks (e.g., Shapiro et al. 2004; Furlanetto & Oh 2005; Sobacchi & Mesinger 2014; Park & Shapiro 2016; D’Aloisio et al. 2020). Furthermore, the λ_{mfp} measurements in B21 are difficult to reconcile with models where reionization completes at $z > 6$, and may instead support models where the IGM is still $\gtrsim 20\%$ neutral at $z = 6$ (B21; Cain et al. 2021; Davies et al. 2021).

Our understanding of how λ_{mfp} evolves over $5 < z < 6$ is highly incomplete, however. The measurements of B21 were restricted to $z \simeq 5.1$ and $\simeq 6.0$ by a lack of high-quality spectra at intermediate redshifts. This was due to a historical redshift gap in the discovery of QSOs near $z \sim 5.5$, which have overlap with brown dwarfs in their visible colors. This gap, however, has been filled by Yang et al. (2017, 2019) using near- and mid-infrared photometry, making it possible to obtain a significant sample of high-quality $z \sim 5.5$ QSO spectra for the first time.

In this work, we report the first measurements of λ_{mfp} at multiple redshifts between $z = 6$ and 5 . In addition to archival

QSO spectra used in B21, our sample includes new QSO spectra from the XQR-30 Very Large Telescope (VLT) large program (e.g., Zhu et al. 2021, 2022; Bischetti et al. 2022; Bosman et al. 2022; Chen et al. 2022; Lai et al. 2022; Davies et al. 2023a; D’Odorico et al. 2023; Satyavolu et al. 2023) as well as from new Keck/Echelle Spectrograph and Imager (ESI) observations. This paper is organized as follows. In Section 2, we describe the data and observations. Section 3 briefly introduces the methods we use to measure λ_{mfp} . We present our results and discuss their implications for reionization in Section 4. Finally, we summarize our findings in Section 5. Throughout this paper we assume a Λ CDM cosmology with $\Omega_{\text{m}} = 0.3$, $\Omega_{\Lambda} = 0.7$, and $h = 0.7$. Distances are quoted in proper units unless otherwise noted. We also use 912 Å to represent the Lyman limit wavelength of 911.76 Å.

2. Data and Observations

To measure λ_{mfp} over $5 < z < 6$, we employ a large sample of 97 spectra of QSOs at $4.9 < z < 6.1$. Our sample includes 23 LRIS spectra and 35 GMOS spectra of QSOs at $z \lesssim 5.3$ used in B21. For higher redshifts, we use 18 and six spectra from the Keck/ESI (Sheinis et al. 2002) and VLT/X-Shooter (Vernet et al. 2011) archives, respectively. We include seven high-quality spectra with sufficient wavelength coverage from the XQR-30 VLT large program (D’Odorico et al. 2023). The rest of the data are new spectra of eight QSOs near $z \sim 5.5$ from our ESI observations. A summary of our QSO sample is provided in Table 1.

In 2021 and 2022, we targeted bright QSOs with z -band magnitude $m_z \leq 20$ presented in Yang et al. (2017, 2019) using ESI. With a typical exposure time of ~ 1 –3 hr and using the 1’’00 and 0’’75 slits, we acquired spectra for 11 objects (Figure 1), including 10 QSOs at $z_{\text{qso}} \sim 5.5$ (eight of them are included in our sample; see below) and one QSO at a lower redshift for replacing its archival spectrum. We followed Becker et al. (2019) to reduce the data, using a custom pipeline that includes optimal techniques for sky subtraction (Kelson 2003), one-dimensional spectral extraction (Horne 1986), and telluric absorption corrections for individual exposures using models based on the atmospheric conditions measured by the Cerro Paranal Advanced Sky Model (Noll et al. 2012; Jones et al. 2013). We extracted the spectra with a pixel size of 15 km s^{-1} . The typical resolution FWHM is approximately 45 km s^{-1} .

All targets in our sample were selected without any foreknowledge of the Lyman continuum (LyC) transmission. We include all usable spectra as long as the QSO is free from very strong associated metal absorption and/or associated Ly α damping wing absorption, which may bias the λ_{mfp} measurements. We also reject objects with strong broad absorption lines near the systemic redshift (see Bischetti et al. 2022 for the XQR-30 spectra). Because the LyC transmission is very weak at $z > 5.3$, we only use spectra with a signal-to-noise ratio (S/N) of $\gtrsim 20$ per 30 km s^{-1} near 1285 Å in the rest frame. Among the objects with new ESI spectra, we exclude J0056 due to its strong associated absorber, and J1236 for its low S/N.

For QSO redshifts, we employ measurements based on submillimeter observations whenever available. Additionally, we carried out Atacama Large Millimeter/submillimeter Array (ALMA) Band 7 observations of our new ESI targets in Cycle 9 and determined the systemic redshifts by fitting the [C II] 158 μm line. For each object, we used two overlapping spectral windows to cover the [C II] line based on the estimated redshift

²⁴ Defined as $\tau_{\text{eff}} = -\ln\langle F \rangle$, where F is the continuum-normalized transmission flux.

Table 1
QSO Spectra Used for λ_{mfp} Measurements

QSO (1)	R.A. (J2000) (2)	Decl. (J2000) (3)	z_{qso} (4)	Ref. (5)	Instrument (6)	M_{1450} (7)	Ref. (8)	R_{eq} (pMpc) (9)
J0015–0049	00:15:29.86	−00:49:04.3	4.931	a	LRIS	−25.2	α	$3.8^{+1.1}_{-0.8}$
J0256+0002	02:56:45.75	+00:02:00.2	4.960	a	LRIS	−24.6	α	$2.8^{+0.9}_{-0.6}$
J0236–0108	02:36:33.83	−01:08:39.2	4.974	a	LRIS	−25.0	α	$3.4^{+1.1}_{-0.7}$
J0338+0018	03:38:30.02	+00:18:40.0	4.988	a	LRIS	−25.1	α	$3.5^{+1.2}_{-0.7}$
J2226–0109	22:26:29.28	−01:09:56.6	4.994	a	LRIS	−24.6	α	$2.8^{+0.9}_{-0.5}$
SDSS J1341+4611	13:41:41.46	+46:11:10.3	5.003	b	GMOS	−25.4	β	$4.0^{+1.3}_{-0.8}$
J0129–0028	01:29:07.45	−00:28:45.6	5.015	a	LRIS	−25.1	α	$3.5^{+1.2}_{-0.7}$
SDSS J1337+4155	13:37:28.82	+41:55:39.9	5.018	b	GMOS	−26.6	β	$7.0^{+2.2}_{-1.4}$
J0221–0342	02:21:12.33	−03:42:31.6	5.024	a	LRIS	−24.9	α	$3.2^{+1.0}_{-0.7}$
SDSS J0846+0800	08:46:27.84	+08:00:51.7	5.028	b	GMOS	−26.9	β	$8.1^{+2.6}_{-1.6}$
J2111+0053	21:11:58.02	+00:53:02.6	5.034	a	LRIS	−25.3	α	$3.9^{+1.2}_{-0.8}$
SDSS J1242+5213	12:42:47.91	+52:13:06.8	5.036	b	GMOS	−25.7	β	$4.7^{+1.5}_{-1.0}$
J0023–0018	00:23:30.67	−00:18:36.6	5.037	a	LRIS	−25.1	α	$3.5^{+1.1}_{-0.7}$
SDSS J0338+0021	03:38:29.31	+00:21:56.2	5.040	b	GMOS	−26.7	β	$7.4^{+2.3}_{-1.5}$
J0321+0029	03:21:55.08	+00:29:41.6	5.041	a	LRIS	−24.9	α	$3.2^{+1.0}_{-0.7}$
SDSS J0922+2653	09:22:16.81	+26:53:59.1	5.042	b	GMOS	−26.0	β	$5.4^{+1.6}_{-1.1}$
SDSS J1534+1327	15:34:59.76	+13:27:01.4	5.043	b	GMOS	−25.0	β	$3.4^{+1.0}_{-0.7}$
SDSS J1101+0531	11:01:34.36	+05:31:33.9	5.045	b	GMOS	−27.7	β	$11.8^{+3.6}_{-2.5}$
SDSS J1340+3926	13:40:15.04	+39:26:30.8	5.048	b	GMOS	−26.8	β	$7.8^{+2.4}_{-1.6}$
SDSS J1423+1303	14:23:25.92	+13:03:00.7	5.048	b	GMOS	−27.1	β	$8.9^{+2.8}_{-1.8}$
SDSS J1154+1341	11:54:24.73	+13:41:45.8	5.060	b	GMOS	−25.6	β	$4.5^{+1.3}_{-1.0}$
J1408+5300	14:08:22.92	+53:00:20.9	5.072	a	LRIS	−25.5	α	$4.3^{+1.3}_{-0.9}$
SDSS J1614+2059	16:14:47.04	+20:59:02.8	5.081	b	GMOS	−26.6	β	$7.2^{+2.0}_{-1.6}$
J2312+0100	23:12:16.44	+01:00:51.6	5.082	a	LRIS	−25.6	α	$4.5^{+1.3}_{-1.0}$
J2239+0030	22:39:07.56	+00:30:22.5	5.092	a	LRIS	−25.2	α	$3.8^{+1.0}_{-0.9}$
SDSS J1204–0021	12:04:41.73	−00:21:49.5	5.094	b	GMOS	−27.4	β	$10.5^{+2.9}_{-2.4}$
J2233–0107	22:33:27.65	−01:07:04.5	5.104	a	LRIS	−25.0	α	$3.5^{+1.0}_{-0.8}$
J0108–0100	01:08:29.97	−01:00:15.7	5.118	a	LRIS	−24.6	α	$2.9^{+0.8}_{-0.7}$
SDSS J1222+1958	12:22:37.96	+19:58:42.9	5.120	b	GMOS	−25.5	β	$4.4^{+1.2}_{-1.0}$
SDSS J0913+5919	09:13:16.55	+59:19:21.7	5.122	b	GMOS	−25.3	β	$4.0^{+1.1}_{-0.9}$
SDSS J1209+1831	12:09:52.71	+18:31:47.0	5.127	b	GMOS	−26.8	β	$8.0^{+2.2}_{-1.8}$
SDSS J1148+3020	11:48:26.17	+30:20:19.3	5.128	b	GMOS	−26.3	β	$6.3^{+1.7}_{-1.5}$
SDSS J1334+1220	13:34:12.56	+12:20:20.7	5.130	b	GMOS	−26.8	β	$8.0^{+2.2}_{-1.9}$
J2334–0010	23:34:55.07	−00:10:22.2	5.137	a	LRIS	−24.6	α	$2.9^{+0.8}_{-0.7}$
J0115+0015	01:15:44.78	+00:15:15.0	5.144	a	LRIS	−25.1	α	$3.7^{+1.0}_{-0.9}$
SDSS J2228–0757	22:28:45.14	−07:57:55.3	5.150	b	GMOS	−26.1	β	$5.8^{+1.6}_{-1.3}$
SDSS J1050+5804	10:50:36.47	+58:04:24.6	5.151	b	GMOS	−26.5	β	$7.0^{+1.9}_{-1.6}$
SDSS J1054+1633	10:54:45.43	+16:33:37.4	5.154	b	GMOS	−26.4	β	$6.6^{+1.8}_{-1.5}$
SDSS J0957+0610	09:57:07.67	+06:10:59.6	5.167	b	GMOS	−27.6	β	$11.6^{+3.1}_{-2.7}$
J2238–0027	22:38:50.19	−00:27:01.8	5.172	a	LRIS	−25.1	α	$3.7^{+1.0}_{-0.8}$
SDSS J0854+2056	08:54:30.37	+20:56:50.9	5.179	b	GMOS	−27.0	β	$8.8^{+2.4}_{-2.1}$
SDSS J1132+1209	11:32:46.50	+12:09:01.7	5.180	b	GMOS	−27.2	β	$9.6^{+2.5}_{-2.2}$
J1414+5732	14:14:31.57	+57:32:34.1	5.188	a	LRIS	−24.8	α	$3.2^{+0.9}_{-0.7}$
SDSS J0915+4924	09:15:43.64	+49:24:16.6	5.199	b	GMOS	−26.9	β	$8.4^{+2.2}_{-1.9}$
SDSS J1221+4445	12:21:46.42	+44:45:28.0	5.203	b	GMOS	−25.8	β	$5.1^{+2.3}_{-0.7}$
SDSS J0824+1302	08:24:54.01	+13:02:17.0	5.207	b	GMOS	−26.2	β	$6.1^{+2.7}_{-0.8}$
J0349+0034	03:49:59.42	+00:34:03.5	5.209	a	LRIS	−25.3	α	$4.1^{+1.8}_{-0.5}$
SDSS J0902+0851	09:02:45.76	+08:51:15.9	5.226	b	GMOS	−25.9	β	$5.4^{+2.3}_{-0.8}$
SDSS J1436+2132	14:36:05.00	+21:32:39.2	5.227	b	GMOS	−26.8	β	$8.2^{+3.3}_{-1.2}$
J2202+0131	22:02:33.20	+01:31:20.3	5.229	a	LRIS	−24.6	α	$3.0^{+1.2}_{-0.5}$
J0208–0112	02:08:04.31	−01:12:34.4	5.231	a	LRIS	−25.3	α	$4.1^{+1.7}_{-0.6}$
J2211+0011	22:11:41.02	+00:11:19.0	5.237	a	LRIS	−24.8	α	$3.3^{+1.3}_{-0.6}$
SDSS J1053+5804	10:53:22.98	+58:04:12.1	5.250	b	GMOS	−27.0	β	$9.3^{+3.5}_{-1.6}$
SDSS J1341+3510	13:41:54.02	+35:10:05.8	5.252	b	GMOS	−26.6	β	$7.7^{+2.9}_{-1.4}$
SDSS J1026+2542	10:26:23.62	+25:42:59.4	5.254	b	GMOS	−26.5	β	$7.4^{+2.7}_{-1.3}$
SDSS J1626+2751	16:26:26.50	+27:51:32.5	5.265	b	GMOS	−27.8	β	$13.6^{+4.7}_{-2.5}$
SDSS J1202+3235	12:02:07.78	+32:35:38.8	5.298	a	ESI	−28.0	β	$15.8^{+4.7}_{-3.5}$

Table 1
(Continued)

QSO (1)	R.A. (J2000) (2)	Decl. (J2000) (3)	z_{qso} (4)	Ref. (5)	Instrument (6)	M_{1450} (7)	Ref. (8)	R_{eq} (pMpc) (9)
SDSS J1233+0622	12:33:33.47	+06:22:34.2	5.300	b	GMOS	-26.2	β	$6.8^{+2.0}_{-1.5}$
SDSS J1614+4640	16:14:25.13	+46:40:28.9	5.313	b	GMOS	-25.8	β	$5.7^{+1.6}_{-1.2}$
SDSS J1659+2709	16:59:02.12	+27:09:35.1	5.316	a	ESI	-27.9	β	$14.6^{+4.2}_{-3.2}$
SDSS J1437+2323	14:37:51.82	+23:23:13.4	5.320	a	ESI	-26.8	β	$9.0^{+2.6}_{-2.1}$
J1656+4541	16:56:35.46	+45:41:13.5	5.336	a	ESI	-27.6	γ	$12.9^{+3.6}_{-2.9}$
SDSS J1340+2813	13:40:40.24	+28:13:28.1	5.349	a	ESI	-26.6	β	$8.3^{+2.3}_{-2.0}$
J0306+1853	03:06:42.51	+18:53:15.8	5.3808	c	ESI ‡	-28.9	γ	$24.5^{+6.6}_{-5.9}$
J0155+0415	01:55:33.28	+04:15:06.7	5.382	a	ESI	-27.0	δ	$10.3^{+2.7}_{-2.5}$
SDSS J0231-0728	02:31:37.65	-07:28:54.5	5.420	a	ESI	-26.6	β	$8.6^{+2.0}_{-2.2}$
J1054+4637	10:54:05.32	+46:37:30.2	5.469	a	ESI ‡	-27.0	δ	$10.3^{+2.3}_{-2.8}$
SDSS J1022+2252	10:22:10.04	+22:52:25.4	5.4787	c	ESI	-27.3	ϵ	$11.9^{+2.4}_{-3.2}$
J1513+0854	15:13:39.64	+08:54:06.5	5.4805	c	ESI ‡	-26.8	δ	$9.6^{+2.0}_{-2.7}$
J0012+3632	00:12:32.88	+36:32:16.1	5.485	c	ESI ‡	-27.2	δ	$11.8^{+2.4}_{-3.0}$
J2207-0416	22:07:10.12	-04:16:56.3	5.5297	c	ESI ‡	-27.8	δ	$15.3^{+7.9}_{-2.6}$
J2317+2244	23:17:38.25	+22:44:09.6	5.5580	c	ESI ‡	-27.4	δ	$12.9^{+6.5}_{-2.2}$
J1500+2816	15:00:36.84	+28:16:03.0	5.5727	c	ESI ‡	-27.6	δ	$14.4^{+6.9}_{-2.6}$
J1650+1617	16:50:42.26	+16:17:21.5	5.5769	c	ESI ‡	-27.2	δ	$12.3^{+5.8}_{-2.3}$
J0108+0711	01:08:06.59	+07:11:20.7	5.580	a	ESI ‡	-27.2	δ	$11.9^{+5.7}_{-2.2}$
J1335-0328	13:35:56.24	-03:28:38.3	5.699	c	X-Shooter	-27.7	δ	$18.0^{+4.1}_{-5.8}$
SDSS J0927+2001	09:27:21.82	+20:01:23.6	5.7722	d	X-Shooter	-26.8	ζ	$12.8^{+1.6}_{-4.8}$
SDSS J1044-0125	10:44:33.04	-01:25:02.2	5.7847	e	ESI	-27.2	η	$15.6^{+1.8}_{-5.9}$
PSOJ 308-27	20:33:55.91	-27:38:54.6	5.798	a	X-Shooter †	-26.8	ζ	$13.3^{+1.3}_{-5.3}$
SDSS J0836+0054	08:36:43.85	+00:54:53.3	5.805	a	ESI	-27.8	ζ	$21.4^{+12.1}_{-5.0}$
SDSS J0002+2550	00:02:39.40	+25:50:34.8	5.824	a	ESI	-27.3	ζ	$17.3^{+9.2}_{-4.2}$
PSOJ 065+01	04:23:50.15	+01:43:24.8	5.8348	f	X-Shooter †	-26.6	ζ	$12.4^{+6.3}_{-3.1}$
PSOJ 025-11	01:40:57.03	-11:40:59.5	5.8414	f	X-Shooter †	-26.9	ζ	$14.4^{+7.4}_{-3.7}$
SDSS J0840+5624	08:40:35.09	+56:24:19.8	5.8441	g	ESI	-27.2	ζ	$16.8^{+8.4}_{-4.4}$
PSOJ 242-12	16:09:45.53	-12:58:54.1	5.8468	f	X-Shooter †	-26.9	ζ	$14.8^{+7.4}_{-3.9}$
PSOJ 023-02	01:32:01.70	-02:16:03.1	5.848	a	X-Shooter †	-26.5	ζ	$12.0^{+6.1}_{-3.0}$
SDSS J0005-0006	00:05:52.33	-00:06:55.6	5.851	a	ESI	-25.7	ζ	$8.4^{+4.1}_{-2.2}$
PSOJ 183-12	12:13:11.81	-12:46:03.5	5.899	a	X-Shooter †	-27.5	ζ	$20.1^{+8.8}_{-5.8}$
SDSS J1411+1217	14:11:11.28	+12:17:37.3	5.920	a	ESI	-26.7	ζ	$12.0^{+5.8}_{-4.1}$
PSOJ 340-18	22:40:48.98	-18:39:43.8	6.0007	h	X-Shooter	-26.4	ζ	$12.4^{+5.1}_{-3.8}$
SDSS J0818+1722	08:18:27.40	+17:22:52.0	6.001	a	X-Shooter	-27.5	ζ	$20.6^{+8.2}_{-6.4}$
SDSS J1137+3549	11:37:17.72	+35:49:56.9	6.030	a	ESI	-27.4	ζ	$19.7^{+8.0}_{-6.0}$
SDSS J1306+0356	13:06:08.26	+03:56:26.2	6.0330	i	X-Shooter	-26.8	ζ	$14.9^{+6.1}_{-4.6}$
ULAS J1207+0630	12:07:37.43	+06:30:10.1	6.0366	j	X-Shooter	-26.6	ζ	$13.6^{+5.4}_{-4.3}$
SDSS J2054-0005	20:54:06.49	-00:05:14.6	6.0391	e	ESI	-26.2	ζ	$11.3^{+4.6}_{-3.5}$
SDSS J0842+1218	08:42:29.43	+12:18:50.6	6.0763	j	X-Shooter †	-26.9	ζ	$15.6^{+6.2}_{-4.9}$
SDSS J1602+4228	16:02:53.98	+42:28:24.9	6.084	a	ESI	-26.9	ζ	$15.6^{+6.2}_{-4.7}$

Notes. Columns: (1) QSO name; (2), (3) QSO coordinates; (4) QSO redshift; (5) reference for QSO redshift; (6) instrument used for λ_{mfp} measurements: † and ‡ denote XQR-30 spectra and spectra from our new ESI observations, respectively; (7) absolute magnitude corresponding to the mean luminosity at rest-frame 1450 Å; (8) reference for M_{1450} ; (9) QSO proximity zone size defined by Equation (2).

References. Redshift lines and references: a. apparent start of the Ly α forest: Becker et al. (2019, 2021) and updated measurements in this work (after correction, see text); b. adopted from Worseck et al. (2014); c. [C II] 158 μm : this work; d. CO: Carilli et al. (2007); e. [C II] 158 μm : Wang et al. (2013); f. [C II] 158 μm : S. E. I. Bosman et al. (2023, in preparation); g. CO: Wang et al. (2010); h. Ly α halo: Farina et al. (2019); i. [C II] 158 μm : Venemans et al. (2020); j. [C II] 158 μm : Decarli et al. (2018). M_{1450} references: α . McGreer et al. (2013, 2018); β . B21, in which M_{1450} values are calculated from the flux-calibrated spectra published by Worseck et al. (2014); γ . Wang et al. (2016); δ . Yang et al. (2017, 2019); ϵ . measured in this work; ζ . Bañados et al. (2016, 2023); η . Schindler et al. (2020).

(This table is available in machine-readable form.)

and another two spectral windows to cover the dust continuum. With C43-(1, 2, 3) configurations, the typical angular resolution is $\sim 1''$. The data are calibrated and reduced using the default procedures of the CASA pipeline (version 6.4.1.12; McMullin et al. 2007; CASA Team et al. 2022). We follow the procedures described in Eilers et al. (2020) to generate the data cube and image the [C II] line: the [C II] emission is continuum-

subtracted with `uvconstsub`, and imaged with the `tclean` procedure using Briggs cleaning and a robust parameter of 2 (natural weighting) to maximize the sensitivity. We use a robust parameter of 0.5 for J1650+1617 to achieve a best data product. The mean rms noise of our data set is 0.25 mJy beam $^{-1}$ per 30 MHz bin. Figure 2 displays [C II] maps along with Gaussian fits to the emission. For each QSO, we

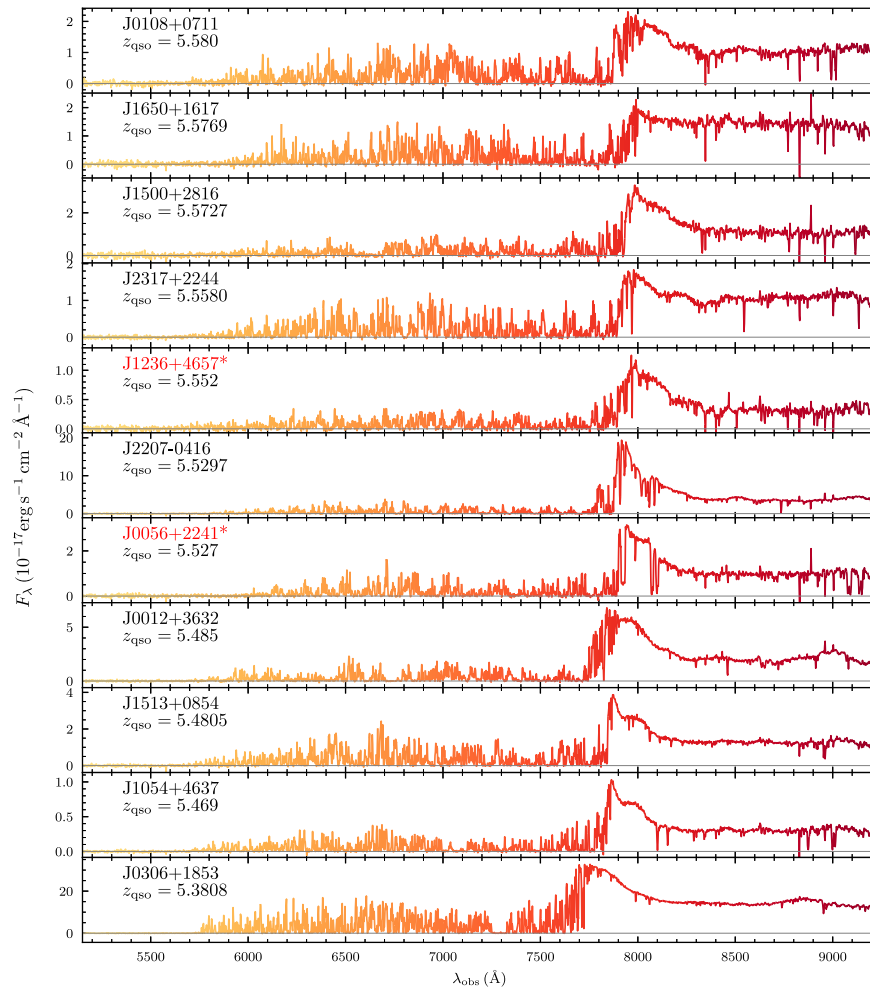


Figure 1. New Keck/ESI QSO spectra obtained for this work. Orange-red and gray curves plot the flux and zero flux, respectively. J0056+2241 and J1236+4657 (labeled with *) are not included in our sample of λ_{mfp} measurements (see text for details). The spectra are rebinned to 2 Å for display.

extract the spectrum within one beam size centered at the target. We create the [C II] map by stacking the data cube within one standard deviation of the Gaussian fit from the line center. We note that the emission line of J0012+3632 is incomplete because the [C II] line is at the edge of our spectral window, which was chosen based on a preliminary redshift estimate (Yang et al. 2019). J1513+0854 shows a double-peak emission line, which may be due to the rotating disk of the QSO host galaxy. Future observations with higher spatial resolution may help resolve the disk.

For the rest of our sample, we employ redshifts measured from the apparent start of the Ly α forest, which are determined for each line of sight by visually searching for the first Ly α absorption line blueward of the Ly α peak (e.g., Worseck et al. 2014; Becker et al. 2019). We do not use redshifts measured from Mg II emission because of their large offsets ($\sim 500 \text{ km s}^{-1}$) from the systemic redshifts (e.g., Venemans et al. 2016; Mazzucchelli et al. 2017; Schindler et al. 2020). Based on 42 QSOs at $5.3 < z_{\text{qso}} < 6.6$ with [C II] or CO redshifts, we find that the redshifts we measure from the apparent start of the Ly α forest are blueshifted from the [C II] or CO redshifts by $\sim 185 \text{ km s}^{-1}$ on average, with a standard deviation of $\sim 370 \text{ km s}^{-1}$. Such a redshift offset can be explained by the strong proximity zone effect close to the QSO: the first significant absorber may typically occur slightly

blueward of the QSO redshift due to ionization effects. This offset is also consistent with that measured in B21. Thus, we shift redshifts measured from the apparent start of the Ly α forest by $+185 \text{ km s}^{-1}$ when measuring λ_{mfp} , and the corrected values are listed in Table 1.

We generate rest-frame composite spectra for QSOs in each $\Delta z = 0.3$ bin, starting from $z = 4.9$. The redshift bins with a mean redshift of $\langle z \rangle = 5.08, 5.31, 5.65$, and 5.93 consist of 44, 26, 9, and 18 spectra, respectively. Following B21, each spectrum is shifted to rest-frame wavelength before being normalized. The normalization is done by dividing each spectrum by its *continuum* flux measured over wavelengths in the rest frame where the flux from broad emission lines is minimal. Here, we use the *continuum* flux over $1270 \text{ Å} < \lambda < 1380 \text{ Å}$ in the rest frame. We have tested that using a different wavelength window does not significantly change our results. Additionally, we identify and mask wavelength regions affected by skyline subtraction residuals. To reject spurious bad pixels, we apply a light median filter using a three-pixel sliding window. Mean composite spectra are then computed in 120 km s^{-1} bins (as shown in the left-hand panel of Figure 3).

3. Methods

We measure λ_{mfp} , which is defined as the distance traveled by ionizing photons that would be attenuated by a factor of $1/e$ by LyC absorption, by fitting the transmitted flux profile

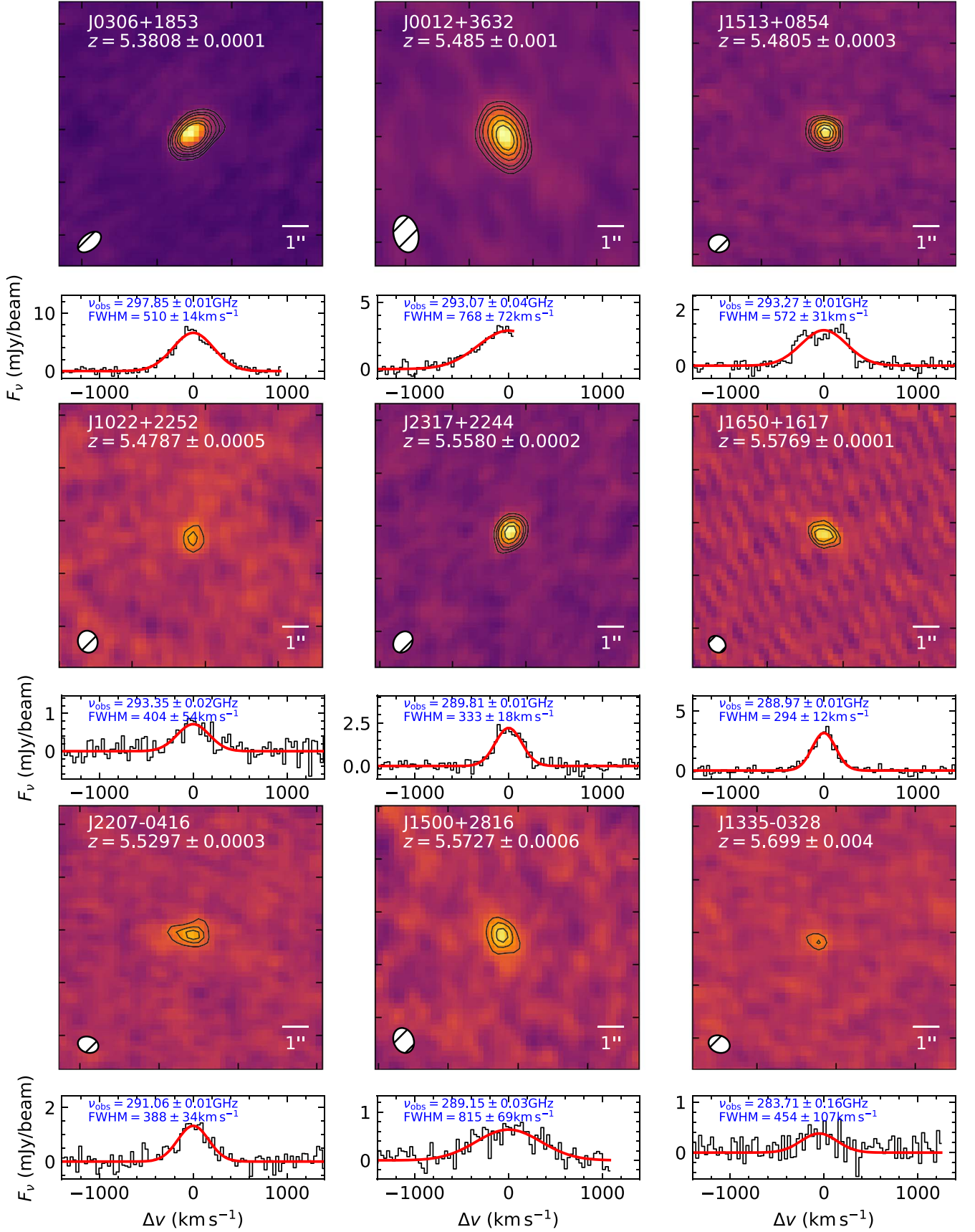


Figure 2. [C II] 158 μm emission maps and spectra of QSOs with our new Keck/ESI observations. Contours show (2σ , 3σ , 4σ , 6σ , 8σ , 10σ) levels. Measured redshifts are labeled for each QSO and red curves show the best Gaussian fits. The observed frequency and FWHM of the [C II] emission are also provided for reference.

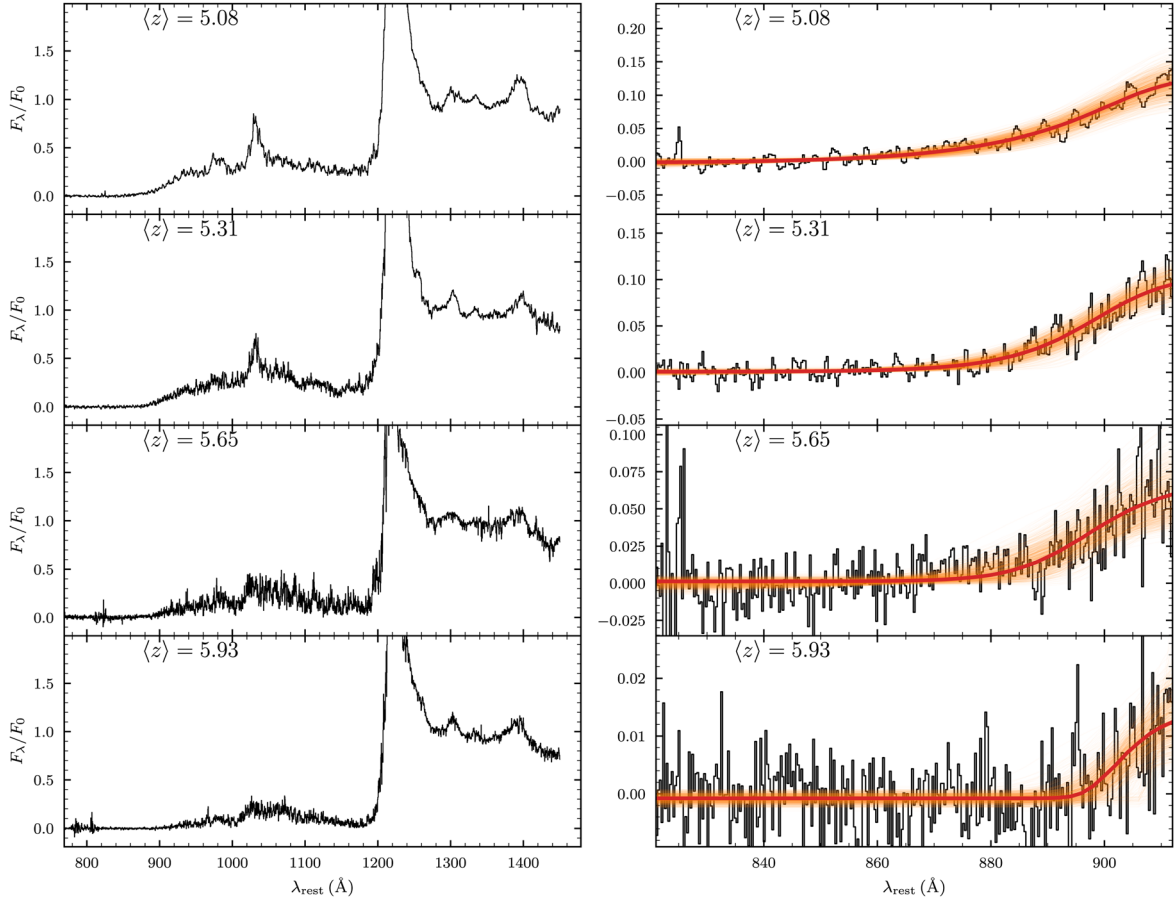


Figure 3. Composite QSO spectra for each redshift bin (left-hand panel) and fits to the LyC transmission (right-hand panel). Black curves show observed flux normalized by the median flux over 1270–1380 Å in the rest frame. The red curve shows our best-fit model. Thin orange curves show the fits from bootstrap realization (only 1000 curves are plotted here for display).

blueward of the Lyman limit in composite QSO spectra (Prochaska et al. 2009; B21). One challenge with this approach is that the LyC transmission at $z > 5$ can be significantly affected by the QSO proximity effect. The ionizing flux from the QSO decreases the ionizing opacity in the proximity zone, which can bias the inferred λ_{mfp} high by a factor of two or more (D’Aloisio et al. 2018; B21). This is especially important when λ_{mfp} is smaller than the proximity zone size, which is true for bright QSOs at $z \gtrsim 5$.

To address this bias, we follow the methods and modeling presented in B21, which modified the Prochaska et al. (2009) method of measuring λ_{mfp} to explicitly include the proximity effect. Motivated by simulations, we account for the decrease in ionizing opacity near the QSO by scaling the opacity, κ_{LL} , according to the local photoionization rate, Γ . This dependence is modeled as a power law such that $\kappa_{\text{LL}} \propto \Gamma^{-\xi}$,

$$\kappa_{\text{LL}}(r) = \kappa_{\text{LL}}^{\text{bg}} \left[1 + \frac{\Gamma_{\text{qso}}(r)}{\Gamma_{\text{bg}}} \right]^{-\xi}, \quad (1)$$

where $\Gamma_{\text{qso}}(r)$ is the photoionization rate due to the QSO at a distance r from the QSO, and Γ_{bg} is the background photoionization rate. In order to calculate $\Gamma_{\text{qso}}(r)$, a key parameter used to describe the proximity zone effect in B21 is R_{eq} . It denotes the distance from the QSO where $\Gamma_{\text{qso}}(r)$ and Γ_{bg} would be equal for purely geometric dilution in the absence of attenuation. Following Calverley et al. (2011), R_{eq} is related

to Γ_{bg} and the ionizing luminosity of the QSO, L_{912} , by

$$R_{\text{eq}} = \left[\frac{L_{912} \sigma_0}{8\pi^2 \hbar \Gamma_{\text{bg}} (\alpha_{\nu}^{\text{ion}} + 2.75)} \right]^{1/2}, \quad (2)$$

where σ_0 and $\alpha_{\nu}^{\text{ion}}$ are the H I ionization cross section at 912 Å and the power-law index of the QSO continuum at $\lambda < 912$ Å in the frequency domain, respectively, and \hbar is the reduced Planck constant. L_{912} can be further related to the absolute magnitude corresponding to the mean luminosity at rest-frame 1450 Å, L_{1450} , by $L_{912} = L_{1450} (\nu_{912}/\nu_{1450})^{-\alpha_{\nu}^{\text{UV}}}$. Here, ν_{912} and ν_{1450} are the photon frequencies at 912 Å and 1450 Å, respectively, and α_{ν}^{UV} is the power-law slope for the non-ionizing (912 Å $< \lambda < 1450$ Å) continuum of the QSO continuum. Following B21, we adopt $\alpha_{\nu}^{\text{ion}} = 1.5 \pm 0.3^{25}$ (Telfer et al. 2002; Stevans et al. 2014; Lusso et al. 2015) and $\alpha_{\nu}^{\text{UV}} = 0.6 \pm 0.1$ (Lusso et al. 2015, see also Vanden Berk et al. 2001; Shull et al. 2012; Stevans et al. 2014).

Following B21, the observed flux, f_{λ}^{obs} , is given by the mean intrinsic QSO continuum, $f_{\lambda}^{\text{cont}} \propto (\lambda/912 \text{ Å})^{\alpha_{\lambda}^{\text{ion}}}$, attenuated by the effective opacity of the Lyman series in the foreground IGM, and the LyC optical depth. The foreground Lyman series

²⁵ $\alpha_{\lambda}^{\text{ion}} = -0.5 \pm 0.3$ in the wavelength domain.

opacity is calculated from

$$\tau_{\text{eff}}^{\text{Lyman}}(\lambda_{\text{obs}}) = \sum_{j=\text{Ly}\alpha, \text{Ly}\beta, \dots, \text{Ly}40} \tau_{\text{eff}}^j(z_j), \quad (3)$$

where $\tau_{\text{eff}}^j(z_j)$ is the effective opacity of transition j at redshift z_j such that $(1+z_j)\lambda_j = \lambda_{\text{obs}}$, and λ_j is the wavelength of transition j in the rest frame. To implement this, we utilized Sherwood simulations (Bolton et al. 2017) to determine the effective optical depth for each Lyman series line across a range of absorption redshifts and Γ values. We then include the proximity zone effect for each Lyman series line by matching the effective optical depth to a Γ value that corresponds to $\Gamma_{\text{bg}} + \Gamma_{\text{qso}}$ as a function of distance from the QSO. We compute Γ_{qso} by dividing the line of sight into small steps of distance δr and solving for $\Gamma_{\text{qso}}(r)$ numerically using the method described in B21. For the first step we assume that Γ_{qso} decreases purely geometrically, i.e.,

$$\Gamma_{\text{qso}}(r = \delta r) = \Gamma_{\text{bg}} \left(\frac{r}{R_{\text{eq}}} \right)^{-2}. \quad (4)$$

We then solve for $\Gamma_{\text{qso}}(r + \delta r)$ over subsequent steps as

$$\Gamma_{\text{qso}}(r + \delta r) = \Gamma_{\text{qso}}(r) \left(\frac{r + \delta r}{r} \right)^{-2} e^{-\kappa_{\text{LL}}(r)\delta r}, \quad (5)$$

where $\kappa_{\text{LL}}(r)$ is computed using Equation (1). Finally, $\tau_{\text{eff}}^j(z_j)$ and $\tau_{\text{eff}}^{\text{Lyman}}(\lambda_{\text{obs}})$ can be computed for each combination of $(\kappa_{\text{LL}}^{\text{bg}}, \xi, z_{\text{qso}}, R_{\text{eq}})$, when fitting to the composite spectra. We have also tested that it does not significantly change the measured λ_{mfp} by either stacking the foreground Lyman series transmission based on z_{qso} and R_{eq} of each individual QSO (as in B21), or computing a total foreground Lyman series transmission based on the averaged z_{qso} and R_{eq} in each redshift bin.

We use the same procedures for parameterizing the LyC transmission as outlined in B21. However, we make one modification by employing the recent measurements of Γ_{bg} from Gaikwad et al. (2023) that match multiple diagnostics of the IGM from observations to the Ly α forest. For reference, the new estimates are $\Gamma_{\text{bg}} \simeq 5 \times 10^{-13} \text{ s}^{-1}$ and $1.5 \times 10^{-13} \text{ s}^{-1}$ at $z = 5.1$ and 6.0 , respectively, in contrast to $7 \times 10^{-13} \text{ s}^{-1}$ and $3 \times 10^{-13} \text{ s}^{-1}$ utilized in B21. The new Γ_{bg} at $z = 5.1$ is also consistent with measurements in, e.g., D’Aloisio et al. (2018). Moreover, instead of assuming a nominal ± 0.15 dex error in Γ_{bg} , we propagate the uncertainties in the measurements of Γ_{bg} from Gaikwad et al. (2023) into R_{eq} . We discuss the effect of Γ_{bg} on λ_{mfp} in Section 4.2.

We fit the transmission for each composite shown in Figure 3 over 820–912 Å in the rest frame. Following B21, uncertainties in λ_{mfp} are estimated using a bootstrap approach wherein we randomly draw QSO spectra with replacement in each redshift bin, and refit the new QSO composites for 10,000 realizations. To account for errors in redshift, we randomly shift the spectrum of each QSO that does not have a submillimeter z_{qso} in redshift following a Gaussian distribution with a standard deviation of 370 km s^{-1} (see Section 2). We include the zero-point as a free parameter while fitting models to the composite, to account for flux zero-point errors. We also treat the normalization of the LyC profile as a free parameter.

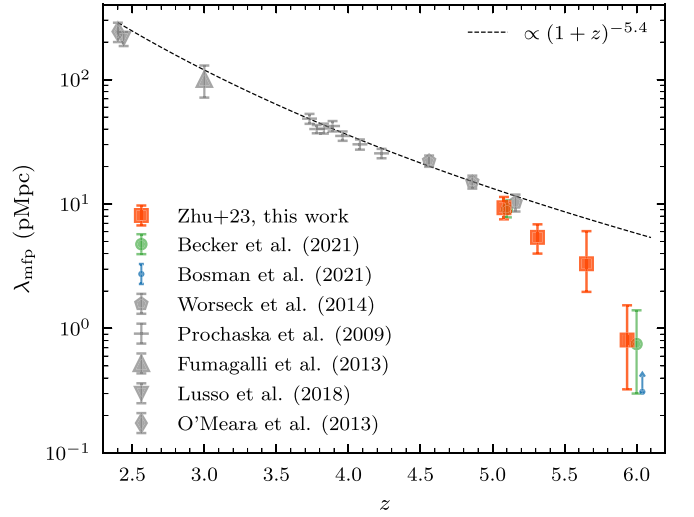


Figure 4. Direct measurements of λ_{mfp} from this work (orange-red squares) and from the literature (Prochaska et al. 2009; Fumagalli et al. 2013; O’Meara et al. 2013; Worseck et al. 2014; Lusso et al. 2018; B21). Error bars show 68% limits. The dashed line shows the power-law extrapolation of λ_{mfp} from measurements at $z < 5.16$ (Worseck et al. 2014). The blue arrow shows the lower-limit constraint on λ_{mfp} at $z = 6$ from Bosman (2021). Symbols are displaced in redshift for display.

We randomly vary ξ by assuming a flat prior over $[0.3, 1.0]$. The fits are shown in the right-hand panel of Figure 3.

4. Results and Discussion

4.1. λ_{mfp} over $5 < z < 6$

We measure $\lambda_{\text{mfp}} = 9.33^{+2.06(3.76)}_{-1.80(2.82)}, 5.40^{+1.47(2.39)}_{-1.40(2.39)}, 3.31^{+2.74(4.02)}_{-1.34(2.06)},$ and $0.81^{+0.73(1.22)}_{-0.48(0.68)}$ pMpc at the averaged redshifts $\langle z \rangle = 5.08, 5.31, 5.65,$ and $5.93,$ respectively. The errors give 68% (95%) confidence limits. Figure 4 plots our results along with previous direct λ_{mfp} measurements from the literature (Prochaska et al. 2009; Fumagalli et al. 2013; O’Meara et al. 2013; Worseck et al. 2014; Lusso et al. 2018; B21). Our measurements at both redshift ends are highly consistent with those presented in B21. Our findings clearly indicate a rapid evolution in λ_{mfp} at $5 < z < 6$, particularly at $z \gtrsim 5.3$.

We have confirmed that using different redshift binning does not significantly affect our results. As the composite spectrum at $\langle z \rangle = 5.65$ includes relatively fewer QSOs, we tested the robustness of our fitting using mock spectra. We created 1000 sets of $N = 9$ mock QSO spectra with similar redshifts and R_{eq} as our sample. The mock spectra were based on our modeling of the transmission at $\lambda < 912 \text{ Å}$, with the mean free path randomly spanning a wide parameter space. We performed 1000 fitting realizations to each of these mock spectra sets, and found that the 68% limits at $z = 5.65$ could recover the simulated confidence level quite well. In addition, it is worth noting that none of the objects in our sample are identified as young QSOs with extremely small proximity zones (e.g., Eilers et al. 2020; Satyavolu et al. 2023), given that the λ_{mfp} values are quite short near $z \sim 6$.

We note that our $\langle z \rangle = 5.65$ stack (Figure 3) includes a small amount of transmission near $\lambda_{\text{rest}} \sim 880 \text{ Å}$, even though the flux has been significantly attenuated at $\lambda_{\text{rest}} > 890 \text{ Å}$. We have inspected each individual spectrum in this redshift bin and have found potential transmission near this wavelength ($\lambda_{\text{obs}} \sim 5800 \text{ Å}$) only in the ESI spectra and not in the X-Shooter spectra.

Table 2
Error Analysis for the Measured λ_{mfp}

	$\langle z \rangle = 5.08$	$\langle z \rangle = 5.31$	$\langle z \rangle = 5.65$	$\langle z \rangle = 5.93$
Measured λ_{mfp}	$9.33^{+2.06}_{-1.80}$	$5.40^{+1.47}_{-1.40}$	$3.31^{+2.74}_{-1.34}$	$0.81^{+0.73}_{-0.48}$
Fixed Γ_{bg} and ξ	$9.33^{+1.95}_{-1.83}$	$5.40^{+1.23}_{-1.14}$	$3.31^{+2.52}_{-0.89}$	$0.81^{+0.45}_{-0.34}$
Varying Γ_{bg} only	$9.33^{+0.43}_{-0.69}$	$5.40^{+0.62}_{-0.72}$	$3.31^{+0.92}_{-0.99}$	$0.81^{+0.21}_{-0.26}$
$\xi = 0.33$	$10.10^{+2.07}_{-1.69}$	$6.57^{+1.23}_{-1.25}$	$5.02^{+1.98}_{-1.32}$	$1.53^{+0.59}_{-0.49}$
$\xi = 0.67$	$9.33^{+2.10}_{-1.81}$	$5.40^{+1.27}_{-1.28}$	$3.31^{+2.67}_{-1.26}$	$0.81^{+0.60}_{-0.40}$
$\xi = 1.00$	$8.74^{+2.18}_{-1.88}$	$4.58^{+1.30}_{-1.33}$	$1.89^{+3.45}_{-0.77}$	$0.30^{+0.66}_{-0.13}$

Notes. λ_{mfp} values are reported in pMpc.

- (1) “Measured λ_{mfp} ,” our λ_{mfp} measurements at each redshift, including all sources of error;
- (2) “Fixed Γ_{bg} and ξ ,” statistical error from bootstrapping the QSO lines of sight without changing the nominal Γ_{bg} or ξ ;
- (3) “Varying Γ_{bg} only,” λ_{mfp} values from varying Γ_{bg} while keeping the QSO lines of sight and ξ fixed;
- (4) Others: λ_{mfp} values based on different fixed ξ values.

This region is at the boundary of two amplifiers of the ESI CCD. It may also be contaminated by scattered light. This feature might therefore be an instrumental issue;²⁶ however, it is also possible that the transmission is real, in which case it may indicate a significant variation in the ionizing free paths toward individual spectra. We hope to explore this in a future work. For the uniform λ_{mfp} model used here, however, our tests based on mock spectra indicate that this transmission feature does not significantly impact our measurements.

4.2. Error Analysis and Dependence on Γ_{bg} and ξ

As described in Section 3, we mitigate the bias on λ_{mfp} from the QSO proximity effect by modeling its impact on the ionizing opacity. The effect is parameterized by a nominal proximity zone size R_{eq} , which specifies the proper distance at which the hydrogen ionization rate due to the QSO would be equal to the background rate in the absence of any attenuation. Therefore, the measured λ_{mfp} has some dependence on R_{eq} . Notably, the uncertainties in R_{eq} listed in Table 1 primarily emanate from Γ_{bg} , with the contribution of uncertainty from α^{UV} and α^{ion} being relatively small ($\lesssim 10\%$). The measurements also depend on ξ , as suggested by Equation (1).

Here, we have examined various sources of error in our λ_{mfp} measurements, including statistical error, error arising from Γ_{bg} , and error stemming from ξ . Specifically, we evaluate the following: (1) the statistical error obtained by bootstrapping the QSO lines of sight while keeping the nominal values of Γ_{bg} and ξ fixed, (2) λ_{mfp} values derived by varying Γ_{bg} while keeping the QSO composite and ξ constant, and (3) λ_{mfp} values obtained for different fixed ξ . Table 2 summarizes the results. We would like to emphasize that fixing any of the parameters to their nominal value can lead to a slightly altered distribution of the resulting λ_{mfp} , and consequently, the corresponding 68% limits may not align precisely with those of the main results. In this case, our primary interest lies in understanding the magnitude of the error.

The “Fixed Γ_{bg} and ξ ” row indicates that the magnitude of the statistical error is comparable to the total error across all

redshifts. This suggests that the dominant factor contributing to the error in our measurements is statistical fluctuations, encompassing factors such as the limited number of QSO spectra, flux noise, uncertainties in redshifts, and uncertainties in α^{UV} and α^{ion} , among others. As shown in the third row, the random fluctuation in Γ_{bg} alone has a minor impact on the overall error. Regarding ξ , the last three rows indicate that using a lower (upper) value of ξ shifts the λ_{mfp} estimates toward higher (lower) face values. This effect is comparable to the statistical fluctuations and is more pronounced at higher redshifts due to the relatively large R_{eq} in comparison to smaller λ_{mfp} . Thus, uncertainties in ξ also make a significant contribution to our λ_{mfp} measurements.

We also explore how our λ_{mfp} measurements depend on Γ_{bg} and ξ *systematically*, such that the results can be easily adjusted for future constraints. Figure 5(a) illustrates the dependence of our best-fitting λ_{mfp} measurements on a wide range of Γ_{bg} values at each redshift. The figure also displays the nominal Γ_{bg} values and their uncertainties. The dependence is minimal at $z \leq 5.3$, where $\lambda_{\text{mfp}} \propto \Gamma_{\text{bg}}^{0.2}$. At these redshifts, the proximity zone size is smaller than or comparable to λ_{mfp} , and hence the measurements are not highly sensitive to Γ_{bg} . At $z \geq 5.6$, however, R_{eq} is similar to or larger than λ_{mfp} , leading to a stronger dependence, with $\lambda_{\text{mfp}} \propto \Gamma_{\text{bg}}^{0.6}$. Nevertheless, if we adopt the higher end of $\Gamma_{\text{bg}} = 3 \times 10^{-13} \text{ s}^{-1}$ at $z = 5.93$, λ_{mfp} would only increase to ~ 1.0 pMpc. The results would remain consistent with a steady and rapid evolution of λ_{mfp} with time.

While there might be an enhanced ionizing background due to galaxies clustering near QSOs, recent research suggests this effect is likely secondary to QSO ionization. Davies (2020) found that even the “ghost” proximity effect of QSOs—a large-scale bias in the mean free path of ionizing photons caused by QSO radiation—could overwhelm the ionizing contribution from the clustering of nearby galaxies. In recent JWST observations, Kashino et al. (2023) also found that the impact of a QSO’s ionizing radiation often dominates over local galactic sources near the QSO. These studies reinforce that, despite potential Γ_{bg} enhancements from galaxy clustering, the QSO’s influence is typically predominant, as adopted in our modeling for the λ_{mfp} measurements.

For our main results, following B21, the mean free path is measured based on a uniform distribution of $\xi \in [0.33, 1.00]$, and the face value is measured for $\xi = 0.67$. As discussed in B21, however, the scaling of κ_{LL} with Γ is highly uncertain, especially for high redshifts. The scaling can be milder (smaller ξ) when neutral islands and/or self-shielding absorbers are present, and steeper (greater ξ) when the IGM shows a more uniform photoionization equilibrium (see, e.g., Furlanetto & Oh 2005; McQuinn et al. 2011; D’Aloisio et al. 2020). For reference, Figure 5(b) shows how our measurements vary with fixed ξ values of 0.33, 0.67, and 1.00. The face value and errors are also listed in Table 2. Similar to the dependence on Γ_{bg} , the measured λ_{mfp} becomes more sensitive to ξ as redshift increases and as the QSO’s proximity effect becomes stronger relative to a smaller λ_{mfp} . Even with the extreme ξ values discussed in B21, nevertheless, the measurements are still consistent with our main results with the 1σ error bars, given the current data. Reassuringly, radiative transfer simulations recently developed by J. T. Roth et al. (2023, in preparation) suggest that the λ_{mfp} inferred using our methods only depends modestly ($\lesssim 20\%$ – 30%) on the QSO lifetimes and environments (see also S. Satyavolu et al. 2023, in preparation). Future

²⁶ Prochaska et al. (2003) also report high flux near $\lambda_{\text{obs}} \sim 5800 \text{ \AA}$ and infer that this is due to an incorrect matching in the gain of the two amplifiers for ESI. We still observe this feature after attempting to carefully account for the gain ratio, however.

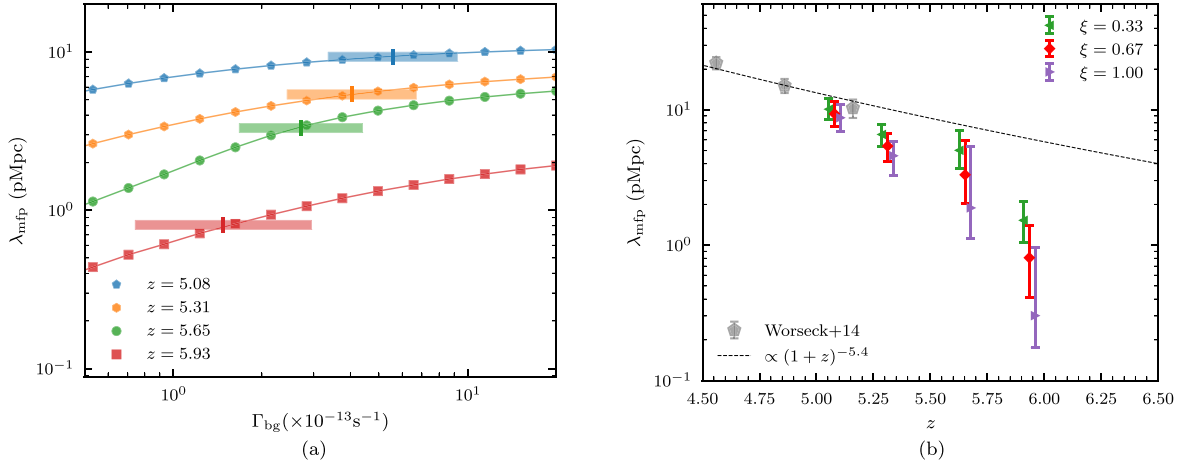


Figure 5. (a) Dependence of the λ_{mfp} measurements on Γ_{bg} at different redshifts. Nominal values and uncertainties of Γ_{bg} we adopt from Gaikwad et al. (2023) are shown with horizontal error bars. (b) Measured λ_{mfp} based on fixed ξ values of 0.33, 0.67, and 1.00. Symbols are displaced in redshift for display.

improved realistic reionization models would provide more insights into the scaling relation, especially when reionization is not fully concluded by $z = 6$.

4.3. Implication for when Reionization Ends

Our measurements not only confirm the λ_{mfp} values presented in B21 at $z = 5.08$ and 5.93 , but also depict a clear evolutionary trend over $5 < z < 6$. The mean free path increases steadily and rapidly with time: λ_{mfp} increases by a factor of ~ 4 from $z \simeq 6.0$ to $z \simeq 5.6$, and by a factor of ~ 2 every $\Delta z = 0.3$ from $z \simeq 5.6$ to $z \simeq 5.0$. This evolution carries important implications for the end of reionization.

D’Aloisio et al. (2020) used radiative transfer hydrodynamic simulations to study the expected evolution of the mean free path following reionization. They found that if reionization had ended well before $z = 6$ and the IGM had sufficient time to relax hydrodynamically, then the evolution would be expected to follow a trend of $\lambda_{\text{mfp}} \propto (1+z)^{-5.4}$. This relation, based on a fully ionized IGM with a homogeneous ionizing ultraviolet background (UVB), is identical to the best-fitting redshift dependence for direct λ_{mfp} measurements at $z \lesssim 5$ (Worseck et al. 2014). However, as shown in Figure 4, this relation significantly overpredicts the measurements by a factor of ~ 2 – 10 over $5.3 < z < 6.0$. By this comparison, the data disfavor a fully ionized and relaxed IGM with a homogeneous UVB at these redshifts.

One possible explanation for the rapid evolution in λ_{mfp} is that reionization ends later than $z = 6$. Such a late-ending reionization scenario has recently been proposed to explain large-scale fluctuations in the observed Ly α effective optical depth (τ_{eff}) at $z > 5$ (e.g., Kulkarni et al. 2019; Keating et al. 2020b; Nasir & D’Aloisio 2020; Choudhury et al. 2021; Qin et al. 2021). The rapid evolution in λ_{mfp} can be naturally explained by ongoing reionization when large ionized bubbles merge and dense, optically thick ionization sinks are photo-evaporated (e.g., Furlanetto & Oh 2005; Sobacchi & Mesinger 2014; D’Aloisio et al. 2020). As mentioned above, the rapid evolution in λ_{mfp} persists as late as $z \lesssim 5.3$, and the significant discrepancy between measurements and predictions from the relaxed IGM model also appears as late as $z = 5.3$. Interestingly, the rapid evolution in λ_{mfp} appears to coincide in redshift with the appearance of large fluctuations in the observed Ly α τ_{eff} at $z \gtrsim 5.3$ (e.g., Becker et al. 2015; Bosman

et al. 2018, 2022; Eilers et al. 2018; Yang et al. 2020b). This may be due to the fact that a shorter λ_{mfp} , along with any potential neutral component from incomplete reionization, will boost the fluctuations in the ionizing UV background, producing scatter in τ_{eff} (e.g., Davies & Furlanetto 2016; Nasir & D’Aloisio 2020; Qin et al. 2021). This joint evolution in the mean free path and UV background is expected near the end of reionization (e.g., Kulkarni et al. 2019; Keating et al. 2020b; Nasir & D’Aloisio 2020). Such a scenario is also consistent with long dark gaps observed in the Ly α /Ly β forest (Zhu et al. 2021, 2022) at $z < 6$, and the fraction of dark pixels measured in the forest (McGreer et al. 2015; Jin et al. 2023).

4.4. Comparison with Reionization Simulations

Figure 6(a) compares our λ_{mfp} measurements to recent numerical simulations of reionization, including the enhanced-sink simulation in Cain et al. (2021), THESAN in Garaldi et al. (2022), and CoDaIII in Lewis et al. (2022). These models use late-ending reionization histories and aim to explain the observed short λ_{mfp} at $z = 6$ and the rapid evolution measured in B21, which we have confirmed in finer detail here. We also include the ATON simulation (“low τ_{CMB} ” model) in Keating et al. (2020a) for reference.

Cain et al. (2021) reproduce λ_{mfp} that is consistent with the $z = 6$ measurements in a late-ending reionization driven by faint galaxies. However, they also find that either a rapid drop in emissivity at $z < 6$ or extra sinks are required to reproduce the λ_{mfp} measurements at $z < 5.2$ in this scenario. Garaldi et al. (2022) use a radiative hydrodynamics simulation and generally reproduce the rapid evolution of λ_{mfp} although they overshoot the $z = 6$ measurement. They find that all of their late-reionization simulations can reproduce a dramatic evolution in λ_{mfp} from $z = 5.5$ to 6 , while one simulation wherein reionization ends by $z > 6$ cannot. Lewis et al. (2022) also find that reionization ending later than $z < 6$ is able to naturally explain the observations. In their CoDa III simulation, this is partly achieved by a drop in cosmic emissivity near the end of reionization driven by strong radiative feedback and high escape fraction in low-mass galaxies (Ocvirk et al. 2021).

We note that these simulations measure λ_{mfp} in slightly different manners. Cain et al. (2021) generate mock LyC QSO spectra using randomly placed sightlines, and fit the stacked spectra using the model proposed by Prochaska et al. (2009).

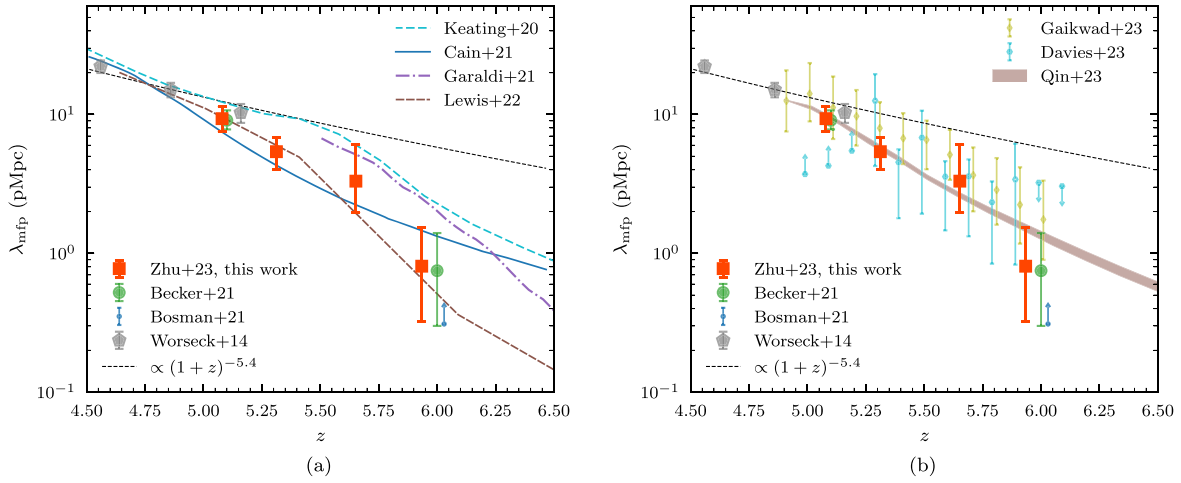


Figure 6. (a) Direct measurements of λ_{mfp} from this work (orange–red squares) compared to the predictions from recent models (Cain et al. 2021; Garaldi et al. 2022; Lewis et al. 2022). (b) Our measurements compared with indirect constraints based on Ly α opacities (Gaikwad et al. 2023; F. B. Davies et al. 2023, in preparation; Y. Qin et al. 2023, in preparation). Open circles correspond to marginal constraints and arrows correspond to 2σ limits for F. B. Davies et al. (2023, in preparation). The shaded region shows the posterior from Y. Qin et al. (2023, in preparation) at the 68% confidence level. In both panels, for comparison, we also show the direct λ_{mfp} measurements in B21 and Worseck et al. (2014), as well as the lower-limit constraint in Bosman (2021). Symbols are displaced in redshift for display.

This procedure mimics the method used in Worseck et al. (2014). On the other hand, Garaldi et al. (2022) measure the distance at which the LyC transmission is attenuated by a factor of $1/e$ from individual sightlines, and take the average. Finally, Lewis et al. (2022) adopted multiple measurement methods for λ_{mfp} , and the curve shown in Figure 6(a) represents the median distance to a $1/e$ attenuation in LyC among sightlines. We also note that the models shown here may not necessarily reproduce observations of the Ly α forest transmission (e.g., Garaldi et al. 2022). Nevertheless, the rapid evolution of λ_{mfp} that we measure over $5 < z < 6$ is broadly consistent with these models that align with a late conclusion to reionization.

4.5. Comparison with Constraints on λ_{mfp} from Ly α Opacities

Recently, Gaikwad et al. (2023) and F. B. Davies et al. (2023, in preparation) have used alternative methods to probe the evolution of λ_{mfp} at these redshifts. Instead of directly measuring λ_{mfp} from the LyC transmission, they use inference methods to jointly constrain λ_{mfp} and Γ_{bg} by modeling the observed Ly α effective optical depth distribution. Specifically, Gaikwad et al. (2023) postprocessed hydrodynamic IGM simulations using a fluctuating UV background specified by a spatially averaged photoionization rate and a mean free path parameter, λ_0 . These variables are constrained by comparing the simulated cumulative distribution function of τ_{eff} with observations using a nonparametric two-sample Anderson–Darlington test. A value of the physical mean free path, λ_{mfp} , is then inferred from the simulated neutral hydrogen distribution once the best-fitting UV background is applied. This step is particularly significant at $z \lesssim 5.3$, where the τ_{eff} distribution is consistent with a uniform UVB (see also Becker et al. 2018; Bosman et al. 2022) and does not constrain λ_{mfp} directly. The fact that the constraints at these redshifts from Gaikwad et al. (2023) agree with the direct constraints presented here suggests that their simulations may be modeling much of the ionizing opacity.

F. B. Davies et al. (2023, in preparation) take a similar approach but use a combination of hydrodynamical and seminumerical simulations to model the density field, and employ a likelihood-free inference technique of approximate

Bayesian computation to constrain λ_{mfp} and Γ_{bg} based on the Ly α forest observations. F. B. Davies et al. (2023, in preparation) also constrain λ_{mfp} by treating it as an “input” subgrid parameter for the UVB fluctuations rather than inferring it from a derived H I density distribution. This accounts for the fact that the F. B. Davies et al. (2023, in preparation) values at $z < 5.3$ are lower limits.

As shown in Figure 6(b), these indirect λ_{mfp} constraints are generally consistent ($\lesssim 1\sigma$) with the direct measurements presented here and in B21. This suggests that the rapidly evolving λ_{mfp} values needed for UV background fluctuations to drive the observed Ly α τ_{eff} distribution are consistent with the attenuation of ionizing photons we observe directly. We note that Gaikwad et al. (2023) and F. B. Davies et al. (2023, in preparation) present somewhat different pictures of the IGM at these redshifts: the Gaikwad et al. (2023) models include neutral islands persisting to $z \simeq 5.2$ while F. B. Davies et al. (2023, in preparation) have the flexibility to vary the λ_{mfp} distribution within ionized regions although no neutral islands are explicitly included. These models are broadly consistent with one another in that the Ly α opacity fluctuations are mainly driven by UV background fluctuations, but this difference highlights the range of physical scenarios that are still formally consistent with the data.

We also include the inference based on multiple observations. Recently, Y. Qin et al. (2023, in preparation) use the 21cmFAST Epoch of Reionization (EoR) simulations (Mesinger et al. 2011; Murray et al. 2020) to constrain IGM properties including its λ_{mfp} . Their input parameters represent galaxy properties such as the stellar-to-halo mass ratio, UV escape fraction, and duty cycles. These allow them to evaluate the UV ionizing photon budget and forward-model the impact on the IGM. Within a Bayesian framework, they include not only the XQR-30 measurement of the forest fluctuations (Bosman et al. 2022) when computing the likelihood but also the CMB optical depth and galaxy UV luminosity functions. Therefore, the posterior they obtain for the IGM mean free path potentially represents a comprehensive constraint from all currently existing EoR observables. As Figure 6(b) displays, the posterior from Y. Qin et al. (2023, in preparation) also

shows a rapid increase in λ_{mfp} with time for $5 \lesssim z \lesssim 6$. Although the posterior does not follow the exact trace of our direct measurements, the general consistency may suggest that such a rapid evolution in λ_{mfp} is potentially favored by other EoR observables.

5. Conclusion

We have presented new measurements of the ionizing mean free path between $z = 5.0$ and 6.0 . These are the first direct measurements in multiple redshift bins over this interval, allowing us to trace the evolution of λ_{mfp} near the end of reionization. Our measurements are based on new and archival data, including new Keck/ESI observations and spectra from the XQR-30 program. By fitting the LyC transmission in composite spectra, we report $\lambda_{\text{mfp}} = 9.33^{+2.06}_{-1.80}$, $5.40^{+1.47}_{-1.40}$, $3.31^{+2.74}_{-1.34}$, and $0.81^{+0.73}_{-0.48}$ pMpc, at $\langle z \rangle = 5.08, 5.31, 5.65$, and 5.93 , respectively. The results confirm the dramatic evolution in λ_{mfp} over $5 < z < 6$, as first reported in B21, and further show a steady and rapid evolution, with a factor of ~ 4 increase from $z \simeq 6.0$ to $z \simeq 5.6$ and a factor of ~ 2 increase every $\Delta z = 0.3$ from $z \simeq 5.6$ to $z \simeq 5.0$. Our λ_{mfp} measurements disfavor a fully ionized and relaxed IGM with a homogeneous UVB at $\gtrsim 95\%$ confidence level down to at least $z \sim 5.3$ and are coincident with the onset of the fluctuations in observed τ_{eff} at $z \sim 5.3$.

Recent indirect λ_{mfp} constraints based on IGM Ly α opacity from Gaikwad et al. (2023) and F. B. Davies et al. (2023, in preparation) agree well with our measurements and those in B21. Our results are also broadly consistent with a range of late-ending reionization models (Cain et al. 2021; Garaldi et al. 2022; Lewis et al. 2022; Gaikwad et al. 2023). Along with other probes from the Ly α and Ly β forests, our results suggest that islands of neutral gas and/or large fluctuations in the UV background may persist in the IGM well below redshift 6.

Acknowledgments

We thank Joshua Roth and Ming-Feng Ho for helpful discussion. We thank the anonymous reviewer for their insightful comments. Y.Z., G.D.B., and H.M.C. were supported by the National Science Foundation through grant AST-1751404. H.M.C. was also supported by the National Science Foundation Graduate Research Fellowship Program under grant No. DGE-1326120. A.D. acknowledges support from NASA 19-ATP19-0191, NSF AST-2045600, and JWST-AR-02608.001-A. S.E.I.B. acknowledges funding from the European Research Council (ERC) under the European Union’s Horizon 2020 research and innovation program (grant agreement no. 740246 “Cosmic Gas”). G.K. is partly supported by the Department of Atomic Energy (Government of India) research project with Project Identification Number RTI 4002, and by the Max Planck Society through a Max Planck Partner Group. M.G.H. acknowledges the support of the UK Science and Technology Facilities Council (STFC) and the National Science Foundation under grant No. NSF PHY-1748958. Y.Q. acknowledges support from the Australian Research Council Centre of Excellence for All Sky Astrophysics in 3 Dimensions (ASTRO 3D), through project #CE170100013. H.U. acknowledges support from JSPS KAKENHI grant No. 20H01953 and 22KK0231.

Based on observations collected at the European Southern Observatory under ESO program 1103.A-0817.

Some of the data presented herein were obtained at the W. M. Keck Observatory, which is operated as a scientific partnership among the California Institute of Technology, the University of California and the National Aeronautics and Space Administration. The Observatory was made possible by the generous financial support of the W. M. Keck Foundation. The authors wish to recognize and acknowledge the very significant cultural role and reverence that the summit of Maunakea has always had within the indigenous Hawaiian community. We are most fortunate to have the opportunity to conduct observations from this mountain. Finally, this research has made use of the Keck Observatory Archive (KOA), which is operated by the W.M. Keck Observatory and the NASA Exoplanet Science Institute (NExSci), under contract with the National Aeronautics and Space Administration.

This paper makes use of the following ALMA data: ADS/JAO.ALMA#2022.1.00662.S, ADS/JAO.ALMA#2021.1.01018.S, and ADS/JAO.ALMA#2019.1.00111.S. ALMA is a partnership of ESO (representing its member states), NSF (USA) and NINS (Japan), together with NRC (Canada), MOST and ASIAA (Taiwan), and KASI (Republic of Korea), in cooperation with the Republic of Chile. The Joint ALMA Observatory is operated by ESO, AUI/NRAO and NAOJ. The National Radio Astronomy Observatory is a facility of the National Science Foundation operated under cooperative agreement by Associated Universities, Inc.

This work has been supported by the Japan Society for the Promotion of Science (JSPS) Grants-in-Aid for Scientific Research (21H01128). This work has also been supported in part by the Sumitomo Foundation Fiscal 2018 Grant for Basic Science Research Projects (180923), the Collaboration Funding of the Institute of Statistical Mathematics “New Perspective of the Cosmology Pioneered by the Fusion of Data Science and Physics.”











For the purpose of open access, the authors have applied a Creative Commons Attribution (CC BY) licence to any Author Accepted Manuscript version arising from this submission.

Facilities: ALMA, Keck:II (ESI), VLT:Kueyen (X-Shooter).

Software: Astropy (Astropy Collaboration et al. 2013), CASA (McMullin et al. 2007; CASA Team et al. 2022), GDL (Coulais et al. 2014), Julia (Bezanson et al. 2017), Matplotlib (Hunter 2007), NumPy (van der Walt et al. 2011), SpectRes (Carnall 2017).

ORCID iDs

Yongda Zhu  <https://orcid.org/0000-0003-3307-7525>
 George D. Becker  <https://orcid.org/0000-0003-2344-263X>
 Holly M. Christenson  <https://orcid.org/0000-0002-0421-065X>
 Sarah E. I. Bosman  <https://orcid.org/0000-0001-8582-7012>
 Tom Bakx  <https://orcid.org/0000-0002-5268-2221>
 Valentina D’Odorico  <https://orcid.org/0000-0003-3693-3091>
 Manuela Bischetti  <https://orcid.org/0000-0002-4314-021X>
 Christopher Cain  <https://orcid.org/0000-0001-9420-7384>
 Frederick B. Davies  <https://orcid.org/0000-0003-0821-3644>
 Rebecca L. Davies  <https://orcid.org/0000-0002-3324-4824>
 Anna-Christina Eilers  <https://orcid.org/0000-0003-2895-6218>
 Xiaohui Fan  <https://orcid.org/0000-0003-3310-0131>
 Prakash Gaikwad  <https://orcid.org/0000-0002-2423-7905>
 Martin G. Haehnelt  <https://orcid.org/0000-0001-8443-2393>

Laura C. Keating  <https://orcid.org/0000-0001-5211-1958>
 Girish Kulkarni  <https://orcid.org/0000-0001-5829-4716>
 Samuel Lai  <https://orcid.org/0000-0001-9372-4611>
 Hai-Xia Ma  <https://orcid.org/0000-0002-5237-9433>
 Andrei Mesinger  <https://orcid.org/0000-0003-3374-1772>
 Yuxiang Qin  <https://orcid.org/0000-0002-4314-1810>
 Sindhu Satyavolu  <https://orcid.org/0000-0001-5818-6838>
 Tsutomu T. Takeuchi  <https://orcid.org/0000-0001-8416-7673>
 Hideki Umehata  <https://orcid.org/0000-0003-1937-0573>
 Jinyi Yang  <https://orcid.org/0000-0001-5287-4242>

References

- Astropy Collaboration, Robitaille, T. P., Tollerud, E. J., et al. 2013, *A&A*, **558**, A33
- Bañados, E., Schindler, J. T., Venemans, B. P., et al. 2023, *ApJS*, **265**, 29
- Bañados, E., Venemans, B. P., Decarli, R., et al. 2016, *ApJS*, **227**, 11
- Bañados, E., Venemans, B. P., Mazzucchelli, C., et al. 2018, *Natur*, **553**, 473
- Becker, G. D., Bolton, J. S., Madau, P., et al. 2015, *MNRAS*, **447**, 3402
- Becker, G. D., D'Aloisio, A., Christenson, H. M., et al. 2021, *MNRAS*, **508**, 1853
- Becker, G. D., Davies, F. B., Furlanetto, S. R., et al. 2018, *ApJ*, **863**, 92
- Becker, G. D., Pettini, M., Rafelski, M., et al. 2019, *ApJ*, **883**, 163
- Bezanson, J., Edelman, A., Karpinski, S., & Shah, V. B. 2017, *SIAM Review*, **59**, 65
- Bischetti, M., Feruglio, C., D'Odorico, V., et al. 2022, *Natur*, **605**, 244
- Boera, E., Becker, G. D., Bolton, J. S., & Nasir, F. 2019, *ApJ*, **872**, 101
- Bolton, J. S., Puchwein, E., Sijacki, D., et al. 2017, *MNRAS*, **464**, 897
- Bosman, S. E. I. 2021, arXiv:2108.12446
- Bosman, S. E. I., Davies, F. B., Becker, G. D., et al. 2022, *MNRAS*, **514**, 55
- Bosman, S. E. I., Fan, X., Jiang, L., et al. 2018, *MNRAS*, **479**, 1055
- CASA Team, Bean, B., & Bhatnagar, S. 2022, *PASP*, **134**, 114501
- Cain, C., D'Aloisio, A., Gangolli, N., & Becker, G. D. 2021, *ApJL*, **917**, L37
- Calverley, A. P., Becker, G. D., Haehnelt, M. G., & Bolton, J. S. 2011, *MNRAS*, **412**, 2543
- Carilli, C. L., Neri, R., Wang, R., et al. 2007, *ApJL*, **666**, L9
- Carnall, A. C. 2017, arXiv:1705.05165
- Chen, H., Eilers, A. C., Bosman, S. E. I., et al. 2022, *ApJ*, **931**, 29
- Choudhury, T. R., Paranjape, A., & Bosman, S. E. I. 2021, *MNRAS*, **501**, 5782
- Christenson, H. M., Becker, G. D., Furlanetto, S. R., et al. 2021, *ApJ*, **923**, 87
- Coulais, A., Schellens, M., Duvert, G., et al. 2014, in ASP Conf. Ser. 485, *Astronomical Data Analysis Software and Systems XXIII* (San Francisco, CA: ASP), 331
- D'Aloisio, A., McQuinn, M., Davies, F. B., & Furlanetto, S. R. 2018, *MNRAS*, **473**, 560
- D'Aloisio, A., McQuinn, M., Trac, H., Cain, C., & Mesinger, A. 2020, *ApJ*, **898**, 149
- Davies, F. B. 2020, *MNRAS*, **494**, 2937
- Davies, F. B., Bosman, S. E. I., Furlanetto, S. R., Becker, G. D., & D'Aloisio, A. 2021, *ApJL*, **918**, L35
- Davies, F. B., & Furlanetto, S. R. 2016, *MNRAS*, **460**, 1328
- Davies, F. B., Hennawi, J. F., Bañados, E., et al. 2018, *ApJ*, **864**, 142
- Davies, R. L., Ryan-Weber, E., D'Odorico, V., et al. 2023a, *MNRAS*, **521**, 289
- Davies, R. L., Ryan-Weber, E., D'Odorico, V., et al. 2023b, *MNRAS*, **521**, 314
- de Belsunce, R., Gratton, S., Coulton, W., & Efstathiou, G. 2021, *MNRAS*, **507**, 1072
- Decarli, R., Walter, F., Venemans, B. P., et al. 2018, *ApJ*, **854**, 97
- D'Odorico, V., Bañados, E., Becker, G. D., et al. 2023, *MNRAS*, **523**, 1399
- Eilers, A. C., Davies, F. B., & Hennawi, J. F. 2018, *ApJ*, **864**, 53
- Eilers, A. C., Hennawi, J. F., Decarli, R., et al. 2020, *ApJ*, **900**, 37
- Fan, X., Strauss, M. A., Becker, R. H., et al. 2006, *AJ*, **132**, 117
- Farina, E. P., Arrigoni-Battaia, F., Costa, T., et al. 2019, *ApJ*, **887**, 196
- Fumagalli, M., O'Meara, J. M., Prochaska, J. X., & Worseck, G. 2013, *ApJ*, **775**, 78
- Furlanetto, S. R., & Oh, S. P. 2005, *MNRAS*, **363**, 1031
- Gaikwad, P., Haehnelt, M. G., Davies, F. B., et al. 2023, arXiv:2304.02038
- Gaikwad, P., Srianand, R., Haehnelt, M. G., & Choudhury, T. R. 2021, *MNRAS*, **506**, 4389
- Garaldi, E., Kannan, R., Smith, A., et al. 2022, *MNRAS*, **512**, 4909
- Greig, B., Mesinger, A., Davies, F. B., et al. 2022, *MNRAS*, **512**, 5390
- Hoag, A. 2019, *ApJ*, **878**, 12
- Home, K. 1986, *PASP*, **98**, 609
- Hu, W., Wang, J., Zheng, Z. Y., et al. 2019, *ApJ*, **886**, 90
- Hunter, J. D. 2007, *CSE*, **9**, 90
- Jin, X., Yang, J., Fan, X., et al. 2023, *ApJ*, **942**, 59
- Jones, A., Noll, S., Kausch, W., Szyzska, C., & Kimeswenger, S. 2013, *A&A*, **560**, A91
- Jung, I., Finkelstein, S. L., Dickinson, M., et al. 2020, *ApJ*, **904**, 144
- Kashino, D., Lilly, S. J., Matthee, J., et al. 2023, *ApJ*, **950**, 66
- Kashino, D., Lilly, S. J., Shibuya, T., Ouchi, M., & Kashikawa, N. 2020, *ApJ*, **888**, 6
- Keating, L. C., Kulkarni, G., Haehnelt, M. G., Chardin, J., & Aubert, D. 2020a, *MNRAS*, **497**, 906
- Keating, L. C., Weinberger, L. H., Kulkarni, G., et al. 2020b, *MNRAS*, **491**, 1736
- Kelson, D. D. 2003, *PASP*, **115**, 688
- Kulkarni, G., Keating, L. C., Haehnelt, M. G., et al. 2019, *MNRAS*, **485**, L24
- Lai, S., Bian, F., Onken, C. A., et al. 2022, *MNRAS*, **513**, 1801
- Lewis, J. S. W., Ocvirk, P., Sorce, J. G., et al. 2022, *MNRAS*, **516**, 3389
- Lusso, E., Fumagalli, M., Rafelski, M., et al. 2018, *ApJ*, **860**, 41
- Lusso, E., Worseck, G., Hennawi, J. F., et al. 2015, *MNRAS*, **449**, 4204
- Mason, C. A., Fontana, A., Treu, T., et al. 2019, *MNRAS*, **485**, 3947
- Mason, C. A., Treu, T., Dijkstra, M., et al. 2018, *ApJ*, **856**, 2
- Mazzucchelli, C., Bañados, E., Venemans, B. P., et al. 2017, *ApJ*, **849**, 91
- McGreer, I. D., Fan, X., Jiang, L., & Cai, Z. 2018, *AJ*, **155**, 131
- McGreer, I. D., Jiang, L., Fan, X., et al. 2013, *ApJ*, **768**, 105
- McGreer, I. D., Mesinger, A., & D'Odorico, V. 2015, *MNRAS*, **447**, 499
- McMullin, J. P., Waters, B., Schiebel, D., Young, W., & Golap, K. 2007, in ASP Conf. Ser. 376, *Astronomical Data Analysis Software and Systems XVI*, ed. R. A. Shaw et al. (San Francisco, CA: ASP), 127
- McQuinn, M., Oh, S. P., & Faucher-Giguère, C. A. 2011, *ApJ*, **743**, 82
- Mesinger, A., Furlanetto, S., & Cen, R. 2011, *MNRAS*, **411**, 955
- Murray, S., Greig, B., Mesinger, A., et al. 2020, *JOSS*, **5**, 2582
- Nasir, F., & D'Aloisio, A. 2020, *MNRAS*, **494**, 3080
- Noll, S., Kausch, W., Barden, M., et al. 2012, *A&A*, **543**, A92
- Ocvirk, P., Lewis, J. S. W., Gillet, N., et al. 2021, *MNRAS*, **507**, 6108
- O'Meara, J. M., Prochaska, J. X., Worseck, G., Chen, H.-W., & Madau, P. 2013, *ApJ*, **765**, 137
- Park, H., & Shapiro, P. R. 2016, *ApJ*, **831**, 86
- Planck Collaboration, Aghanim, N., & Akrami, Y. 2020, *A&A*, **641**, A6
- Prochaska, J. X., Gawiser, E., Wolfe, A. M., Cooke, J., & Gelino, D. 2003, *ApJS*, **147**, 227
- Prochaska, J. X., Worseck, G., & O'Meara, J. M. 2009, *ApJL*, **705**, L113
- Qin, Y., Mesinger, A., Bosman, S. E. I., & Viel, M. 2021, *MNRAS*, **506**, 2390
- Satyavolu, S., Eilers, A. C., Kulkarni, G., et al. 2023, *MNRAS*, **522**, 4918
- Schindler, J. T., Farina, E. P., Bañados, E., et al. 2020, *ApJ*, **905**, 51
- Shapiro, P. R., Iliev, I. T., & Raga, A. C. 2004, *MNRAS*, **348**, 753
- Sheinis, A. I., Bolte, M., Epps, H. W., et al. 2002, *PASP*, **114**, 851
- Shull, J. M., Stevans, M., & Danforth, C. W. 2012, *ApJ*, **752**, 162
- Sobacchi, E., & Mesinger, A. 2014, *MNRAS*, **440**, 1662
- Stevans, M. L., Shull, J. M., Danforth, C. W., & Tilton, E. M. 2014, *ApJ*, **794**, 75
- Telfer, R. C., Zheng, W., Kriss, G. A., & Davidsen, A. F. 2002, *ApJ*, **565**, 773
- van der Walt, S., Colbert, S. C., & Varoquaux, G. 2011, *CSE*, **13**, 22
- Vanden Berk, D. E., Richards, G. T., Bauer, A., et al. 2001, *AJ*, **122**, 549
- Venemans, B. P., Walter, F., Neeleman, M., et al. 2020, *ApJ*, **904**, 130
- Venemans, B. P., Walter, F., Zschaechner, L., et al. 2016, *ApJ*, **816**, 37
- Vernet, J., Dekker, H., D'Odorico, S., et al. 2011, *A&A*, **536**, A105
- Wang, F., Davies, F. B., Yang, J., et al. 2020, *ApJ*, **896**, 23
- Wang, F., Wu, X. B., Fan, X., et al. 2016, *ApJ*, **819**, 24
- Wang, R., Carilli, C. L., Neri, R., et al. 2010, *ApJ*, **714**, 699
- Wang, R., Wagg, J., Carilli, C. L., et al. 2013, *ApJ*, **773**, 44
- Weinberger, L. H., Haehnelt, M. G., & Kulkarni, G. 2019, *MNRAS*, **485**, 1350
- Wold, I. G. B., Malhotra, S., Rhoads, J., et al. 2022, *ApJ*, **927**, 36
- Worseck, G., Prochaska, J. X., O'Meara, J. M., et al. 2014, *MNRAS*, **445**, 1745
- Yang, J., Fan, X., Wu, X. B., et al. 2017, *AJ*, **153**, 184
- Yang, J., Wang, F., Fan, X., et al. 2019, *ApJ*, **871**, 199
- Yang, J., Wang, F., Fan, X., et al. 2020a, *ApJL*, **897**, L14
- Yang, J., Wang, F., Fan, X., et al. 2020b, *ApJ*, **904**, 26
- Zhu, Y., Becker, G. D., Bosman, S. E. I., et al. 2021, *ApJ*, **923**, 223
- Zhu, Y., Becker, G. D., Bosman, S. E. I., et al. 2022, *ApJ*, **932**, 76